PCCP

PAPER

View Article Online
View Journal | View Issue

Cite this: *Phys. Chem. Chem. Phys.*, 2024, **26**, 3632

Effect of temperature on the gas-phase reaction of CH_3CN with OH radicals: experimental (T = 11.7–177.5 K) and computational (T = 10–400 K) kinetic study†

Daniel González, [ab] André Canosa, [c] Emilio Martínez-Núñez, [d] Antonio Fernández-Ramos, *[de] Bernabé Ballesteros, [ab] Marcelino Agúndez, [f] José Cernicharo [f] and Elena Jiménez *[ab]

Acetonitrile (CH_3CN) is present in the interstellar medium (ISM) in a variety of environments. However, at the ultracold temperatures of the ISM, radical-molecule reactions are not widely investigated because of the experimental handicap of getting organic molecules in the gas phase by conventional techniques. The CRESU (French acronym for Reaction Kinetics in a Uniform Supersonic Flow) technique solves this problem. For this reason, we present in this work the kinetic study of the gas-phase reaction of CH_3CN with one of the most ubiquitous radicals, the hydroxyl (OH) radical, as a function of temperature (11.7–177.5 K). The kinetic technique employed to investigate the CH_3CN + OH reaction was the pulsed laser photolysis-laser induced fluorescence. The rate coefficient for this reaction $k(T)$ has been observed to drastically increase from 177.5 K to 107.0 K (about 2 orders of magnitude), while the increase in $k(T)$ from 107.0 K to 11.7 K was milder (around 4 times). The temperature dependent expressions for $k(T)$ are provided in the two distinct T-ranges, excluding the upper limit obtained for k(177.5 K):

$$k(11.7-135.0\ \mathrm{K}) = (1.50 \pm 0.12) \times 10^{-11} \left(\frac{T}{300\ \mathrm{K}}\right)^{-(0.53\pm0.03)}\ \mathrm{cm^3\ s^{-1}}$$

$$k(135.0-149.9\ \mathrm{K}) = (1.50 \pm 1.48) \times 10^{-20} \left(\frac{T}{300\ \mathrm{K}}\right)^{-(26.4\pm1.5)}\ \mathrm{cm^3\ s^{-1}}.$$

In addition, the rate coefficients estimated by the canonical competitive unified statistical (CCUS) theory show a similar behaviour to the experimental results, when evaluated within the high-pressure limit. This is consistent with the experimentally observed independence of $k(T)$ with total gas density at selected temperatures. Astrochemical networks, such as the KIDA database or UMIST, do not include the CH_3CN + OH reaction as a potential depletion process for acetonitrile in the ISM because the current studies predict very low rate coefficients at IS temperatures. According to the model (T = 10 K), the impact of the titled reaction on the abundances of CH_3CN appears to be negligible in dark molecular clouds of the ISM (~1% of the total depletion reactions included in UMIST network). With respect to the potential formation of the CH_2CN radical in those environments, even in the most favourable scenario, where this radical could be formed in a 100% yield from the CH_3CN + OH reaction, this route would only contribute around 2% to the current assumed formation routes by the UMIST network.

Received 11th October 2023,
Accepted 5th January 2024

DOI: 10.1039/d3cp04944b

rsc.li/pccp

[a] *Departamento de Química Física, Facultad de Ciencias y Tecnologías Químicas, Universidad de Castilla-La Mancha (UCLM), Avda. Camilo José Cela 1B, 13071 Ciudad Real, Spain. E-mail: Elena.Jimenez@uclm.es*
[b] *Instituto de Investigación en Combustión y Contaminación Atmosférica, UCLM, Camino de Moledores s/n, 13071 Ciudad Real, Spain*
[c] *Institut de Physique de Rennes-CNRS – UMR 6251, Université de Rennes, F-35000 Rennes, France*
[d] *Departamento de Química Física, Facultade de Química, Campus Vida, Universidade de Santiago de Compostela, Avda. das Ciencias s/n, 15782, Santiago de Compostela, Spain. E-mail: qf.ramos@usc.es*
[e] *Centro Singular de Investigación en Química Biológica y Materiales Moleculares (CIQUS), Campus Vida, Universidade de Santiago de Compostela, C/Jenaro de la Fuente s/n, 15782, Santiago de Compostela, Spain*
[f] *Molecular Astrophysics Group, Instituto de Física Fundamental (IFF-CSIC), Consejo Superior de Investigaciones Científicas, C/Serrano 123, 28006, Madrid, Spain*
† Electronic supplementary information (ESI) available. See DOI: https://doi.org/10.1039/d3cp04944b

1. Introduction

Acetonitrile, also known as methyl cyanide (CH_3CN), is the simplest organic nitrile molecule. This N-bearing species is present in natural environments such as the Earth's atmosphere, solar system objects, interstellar matter, and even nearby galaxies. This prolate symmetric-top molecule is well-suited for millimetre-wave observations due to its large permanent dipole moment ($\sim$4 Debye).[1] Regarding the terrestrial atmosphere, CH_3CN is a trace gas, essentially issued from biomass burning.[2] Its lifetime in the troposphere is about 6 months with deposition in the ocean being the dominant removal process. Therefore, it can be transported to the stratosphere where it can stay for several decades.[3] The reaction with the hydroxyl (OH) radical becomes the main sink.

In the context of the search for the origin of life, a main concern in modern astrochemistry and astrobiology, CH_3CN is of special interest for prebiotic evolution because of the main role played by C–N bonds in the formation of peptide structures, such as amino acids. Then, CH_3CN has been searched and detected routinely in a large variety of extraterrestrial environments, becoming one of the most abundant complex organic molecules (COMs) ever seen in space. In the solar system, CH_3CN has been frequently observed in comets,[4] for instance in Kohoutek,[5] Hale-Bopp,[6,7] P/Halley[8] or 67P/Churyumov–Gerasimenko.[9] It has also been identified in one of Saturn's moons, Titan, either by ground-based observations[10] or *in situ* measurements.[11] In the interstellar medium (ISM), CH_3CN is one of the few prebiotic molecules seen in all main phases of the lifetime cycle of stars from the early stages to the last remnants. Since its first detection towards SgrA and SgrB molecular clouds in 1971,[12] it has been observed in diffuse and translucent clouds,[13–15] dark clouds,[16] photodissociation regions,[17,18] circumstellar envelopes,[19,20] hot cores,[21,22] protostellar objects,[23,24] protoplanetary disks[25,26] or molecular outflows[27,28] as well as in extragalactic sources.[29,30] In addition, CH_3CN is a good thermometer for interstellar gas[31,32] and a useful tracer of shocks[33,34] and kinematic structures.[28] Its gas-phase formation routes have been very recently discussed by Giani *et al.*[35] As it can be seen, CH_3CN is a quite important molecule in the different surroundings of the ISM, including those where the ultra-low temperatures (10–100 K) prevail. For that reason, it is essential to simulate this cold environment in the laboratory to study the gas-phase reactivity of CH_3CN towards the most abundant radicals in the ISM, like the OH radical which plays a significant role in many chemical processes.[36–39] Nevertheless, although the CH_3CN + OH reaction (reaction (1)) has been quite extensively studied both experimentally at $T > 250$ K[40–48] and theoretically at $T > 200$ K,[49–52] it has never been investigated at the ultralow temperatures of the ISM.

$$CH_3CN + OH \rightarrow \text{Products} \quad k(T) \qquad (1)$$

In summary, the experimental kinetic studies of reaction (1) were performed in a wide range of pressures (P = 1.2–760 Torr) and temperatures (T = 250–424 K) using various techniques (see Table 1). Both absolute[40–45] and relative[47,48] kinetic techniques were employed to determine the rate coefficient $k(T)$ of reaction (1) at a temperature T. At room temperature, k(298 K) has been reported in single temperature experiments[42,43,46,48] or as part of the temperature dependence study of reaction (1).[40,41,44,45,47] Most of the studies are in agreement, except the ones by Harris *et al.*[40] and Andersen *et al.*,[48] the most recent experimental study, whose k(298 K) both differ by a factor of about 2 with previous measurements. As shown in Table 1, there are several studies on the pressure dependence of k(298 K).[43–45] Kurylo and Knable[44] observed a 10% increase of the rate coefficient in the range 20–50 Torr of either argon or SF_6, while Zetzsch[43] found, according to Hynes and Wine,[45] an increase of k(298 K) by a factor of 2.5 in the pressure range 5–100 Torr of argon. However, k(298 K) reported by Poulet *et al.*[41] at 1.2 Torr of He is in agreement with high-pressure results. This was confirmed

Table 1 Synthetic view of the available literature for the CH_3CN + OH reaction: experiments. The temperature dependence of the rate coefficient for reaction (1) is mathematically fitted by the modified Arrhenius expression: $k(T) = A \times \left(\frac{T}{298\text{ K}}\right)^n \times \exp^{-\frac{\gamma}{T}}$

P/Torr	Buffer gas	T/K	Method[a]	k(298 K)/10^{-14} cm^3 s^{-1}	A/10^{-13} cm^3 s^{-1}	n	γ/K	Products	Ref.
50	Ar	297–424	FP-RF	4.94 ± 0.6	5.86	0	756 ± 126	H-Abst deduced	Harris *et al.*[40]
7	Ar	295	FP-RF	2.4 ± 0.3				H-Abst assumed	Fritz *et al.*[42]
5–100	Ar	298	FP-RF	1.9 ± 0.2[b]				—	Zetzsch[43]
1.2	He	295 393	DF-EPR	2.1 ± 0.3				H-Abst deduced	Poulet *et al.*[41]
20; 50	Ar SF_6	250–363	FP-RF	1.94 ± 0.37	6.28	0	1030	H-Abst deduced	Kurylo and Knable[44]
50–700 N_2 30–600 He (298 K)	N_2 N_2/O_2 He	256–388	PLP-LIF	2.48 ± 0.38	11	0	1130 ± 90	~50% H-Abst ~50% OH Ad.	Hynes and Wine[45]
700	Air	296	Smog chamber FTIR					~50% H-Abst.[d] ~50% OH Ad.	Tyndall *et al.*[46]
760	Ar	306–393	FP-FTIR	1.82	18.5	0	1377 ± 62	H-Abst deduced	DeMore[47]
700	Air	296	Smog chamber FTIR	4.07 ± 1.21[c]				H-Abst assumed	Andersen *et al.*[48]

[a] Flash photolysis resonance fluorescence (FP-RF); discharge flow coupled to electron paramagnetic resonance (DF-EPR); pulsed laser photolysis-laser-induced fluorescence (PLP-LIF); Fourier transform infrared (FTIR). [b] From Hynes and Wine[45] at about 100 Torr. [c] Average rate coefficients using different reference compounds. [d] Indirectly deduced from HC(O)CN quantification.

later by Hynes and Wine,[45] who essentially found no pressure dependence of k(298 K) between 30 and 700 Torr, neither in N_2 nor in He.

Concerning the temperature dependence of $k(T)$, a positive activation energy has been reported between 250 and 424 K, *i.e.*, $k(T)$ decreases when temperature decreases. The Arrhenius parameters reported by Harris *et al.*,[40] derived from kinetic data obtained at temperatures above room temperature, were slightly lower than those obtained by Kurylo and Knable,[44] Hynes and Wine[45] and DeMore *et al.*,[47] whose temperature dependences were essentially identical. Harris *et al.*[40] and Kurylo and Knable[44] interpreted the observed normal Arrhenius behaviour as a prevalence of the H-abstraction from the methyl group of acetonitrile (channel (1a)):

$$CH_3CN + OH \rightarrow CH_2CN + H_2O \quad (1a)$$

Nevertheless, Hynes and Wine,[45] from a series of experiments in a mixture of O_2 and N_2, found indirect evidence that the OH-addition accounted for about 50% of the total reaction process at room temperature. This branching ratio was later confirmed by Tyndall *et al.*[46] in smog chamber experiments at 700 Torr.

$$CH_3CN + OH \rightarrow CH_3C(OH)N \quad (1b)$$

$$\rightarrow CH_3CN(OH) \quad (1c)$$

From a theoretical point of view, the potential energy surfaces (PES) of various routes from reactant to products[49–52] were investigated by diverse methods (see Table 2), and from the obtained PES the temperature dependence of $k(T)$[51–53] was calculated using different variants of the general transition state theory (TST). Li and Wang[53] calculated the rate coefficient for the reaction pathway (1a), $k_{1a}(T)$, in the temperature range 250–2500 K using the canonical variational TST (CVT) with a small curvature tunnelling (SCT) correction. The calculated k(298 K) was found to agree with several experiments.[41,44,45] As mentioned earlier, the contribution of the OH-addition channels to $k(T)$ was not negligible. Thus, the OH-addition channels were theoretically investigated by Galano,[50] concluding that reaction (1c) was endothermic while reaction paths (1a) and (1b) have similar efficiency, based on close Gibbs free energy barriers. No rate coefficients were calculated, however. Additional reaction pathways were explored by Tian *et al.*[51] concluding that reaction channel (1a) was the dominant one whereas the two OH-addition channels were not considered as terminal in the reaction pathways. The rate coefficient $k_{1a}(T)$ was calculated using TST with the Wigner correction to take tunnelling into account. At room temperature their calculation agreed well with the measurements from Harris *et al.*[40] and Andersen *et al.*[48] More recently, Alihosseini *et al.*[52] found 12 viable routes along the PES of the OH + CH_3CN reaction. Only the rate coefficient $k_{1a}(T)$ was calculated using TST, at atmospheric pressure over the temperature range of 200–2500 K. In this temperature range, a non-Arrhenius behaviour of $k_{1a}(T)$ was predicted, however the authors fitted the data to a conventional Arrhenius equation which gives a very poor representation of individual $k_{1a}(T)$ (see Fig. 5 in Alihosseini *et al.*[52]). Furthermore, k_{1a}(298 K) is about two orders of magnitude higher (2.17×10^{-12} cm^3 s^{-1}) than previous investigations either experimental or theoretical.

Therefore, there are still matters of controversy concerning the rate coefficient $k(T)$, the branching ratios, and the influence of pressure in the obtained measures. In addition, the extension of experimental and theoretical studies to temperatures lower than 200 K is certainly desirable, especially for the modelling of the chemistry of interstellar objects in which CH_3CN and OH have been observed. Astrochemical networks, such as the KIDA database or UMIST, do not include reaction (1) as a potential depletion process for acetonitrile in the ISM. The present investigation aims at studying the gas-phase kinetics of the CH_3CN + OH reaction between 11.7 K and 177.5 K from an experimental point of view using a pulsed CRESU (French acronym for Reaction Kinetics in a Uniform Supersonic Flow) reactor and from a theoretical point of view using high level quantum chemistry tools such as the density functional theory (DFT) and the competitive canonical unified theory (CCUS) in the temperature range of 10–400 K. The results reported here were used to model the IS abundance of CH_3CN using a pure gas-phase astrochemical model and the implications of our results in the chemistry of IS molecular clouds are discussed.

Table 2 Synthetic view of the available literature for the CH_3CN + OH reaction: theory. The temperature dependence of the rate coefficient is mathematically fitted by the modified Arrhenius expression: $k(T) = A \times \left(\frac{T}{298\ \mathrm{K}}\right)^n \times \exp^{-\frac{\gamma}{T}}$

Method	T (K)	k(298 K)/ 10^{-14} cm^3 s^{-1}	A[a]/ 10^{-13} cm^3 s^{-1}	n	γ (K)	Products	Ref.
PMP4/6-311_G(2df,2pd)//MP2/6-311G(d,p)	250–2500	2.38[a]	1.4[b]	2.89[b]	620[b]	H-Abst only considered	Li and Wang[53]
QCISD(T)/6-311_G(2df,2pd)//MP2/6-311G(d,p) + CVTST/SCT	250–2500	2.02[a]	1.3[b]	2.91[b]	648[b]	H-Abst only considered	Li and Wang[53]
BHandHLYP/6-311++G(2d,2p) + CCSD(T)/6-311++G(2d,2p)	—	—	—	—	—	~50% H-Abst ~50% OH Ad.	Galano[50]
B3LYP/CBSB7 TST + Wigner correction	250–3000	5.14	7.05	3.045	−780	7 routes obtained H-Abst mainly	Tian *et al.*[51]
CBS-QB3 TST + Wigner correction	250–430	4.79	15.6	2.36	−1038	7 routes obtained H-Abst mainly	Tian *et al.*[51]
B3LYP + G3B3 or CCSD(T)/6-311++G(3df,3pd) + TST	200–2500	217	489	0	−1277	12 routes obtained but H-Abst only considered	Alihosseini *et al.*[52]

[a] Calculated at 298 K (not from fit). [b] Obtained in the present work from the data presented in Table 5 from Li and Wang.[53]

2. Experimental part

The kinetic study of reaction (1) has been performed at ultralow temperatures (11.7–177.5 K) achieved by a pulsed CRESU apparatus, where the gas is not continuously passing through the Laval nozzle. A detailed description of the technique and the set-up can be found elsewhere.[54–61] Hence, a schematic diagram with the experimental novelties of the present work is provided in Scheme 1 and only a brief description is given below.

Seven different Laval nozzles and a total of 15 operational conditions were used in this work to fill up the temperature range. The isentropic expansion from a relative high-pressure reservoir (P_{res} = 9.97–366.48 mbar) to a low-pressure chamber (0.12–6.00 mbar) through the nozzle results in a uniform supersonic cold jet ranging from 11.7 and 177.5 K. A rotary disk with one or two symmetrical apertures was employed to pulse the gas at 5 Hz for T = 11.7 K or 10 Hz for the rest of operational conditions, respectively.

The kinetic technique pulsed laser photolysis-laser-induced fluorescence (PLP-LIF) was also described previously.[54,55,59,62–68] The production of OH radicals along the supersonic jet was achieved by PLP of gaseous H_2O_2 or *tert*-butyl hydroperoxide (*t*-BuOOH) at 248 nm, radiation generated by a KrF excimer laser (Coherent, model ExciStar XS 200). Both precursors were introduced in the reservoir by flowing a small portion of the buffer gas (He, N_2, or Ar) through the bubbler containing the concentrated solution of the OH precursor (see Scheme 1). Gaseous CH_3CN was introduced in the reservoir by flowing diluted mixtures in the buffer gas through a calibrated mass flow controller (method 1) or by bubbling liquid samples of CH_3CN with a small portion of the buffer gas (method 2). More details of both methods are given in the ESI.† Once the OH radicals were generated in the electronic ground state, they were excited at *ca.* 282 nm, radiation achieved with a frequency-doubled dye laser (Lambda Physik, model Scanmate) pumped by the second harmonic of a Nd:YAG laser (Continuum, model Surelite III). Finally, the temporal evolution of OH radicals in the presence and absence of acetonitrile was monitored by LIF (I_{LIF}) at *ca.* 310 nm, using a photomultiplier tube (Electron Tube, model 9813B) with a bandpass filter centred at 310 nm with a full width at half maximum of 10 nm (Andover Co., model 310FS10-25).

2.1. Kinetic analysis

The kinetic experiments were performed under pseudo-first order conditions, *i.e.*, in large excess of acetonitrile with respect to the initial concentration of OH radicals ($[CH_3CN] \gg [OH]_0$). In such a situation, after an increase due to rotational relaxation (see ESI† and already explained),[54,57] the temporal profile of I_{LIF} results in an exponential decay primarily caused by the reaction of OH with CH_3CN, but also by the reaction with the OH-precursor (H_2O_2 or *t*-BuOOH) or diffusion out of the detection zone. Some examples of the temporal profile of I_{LIF} recorded in the absence and presence of CH_3CN at three selected temperatures are shown in Fig. S1 of ESI.† From the analysis of the I_{LIF} decays, the pseudo-first order rate coefficient, k' (or k'_0 in the absence of CH_3CN) was obtained. In these experimental conditions, k' is proportional to $[CH_3CN]$ at a single temperature, according to the relationship given by eqn (E1):

$$k' = k(T)[CH_3CN] + k'_0 \quad \text{(E1)}$$

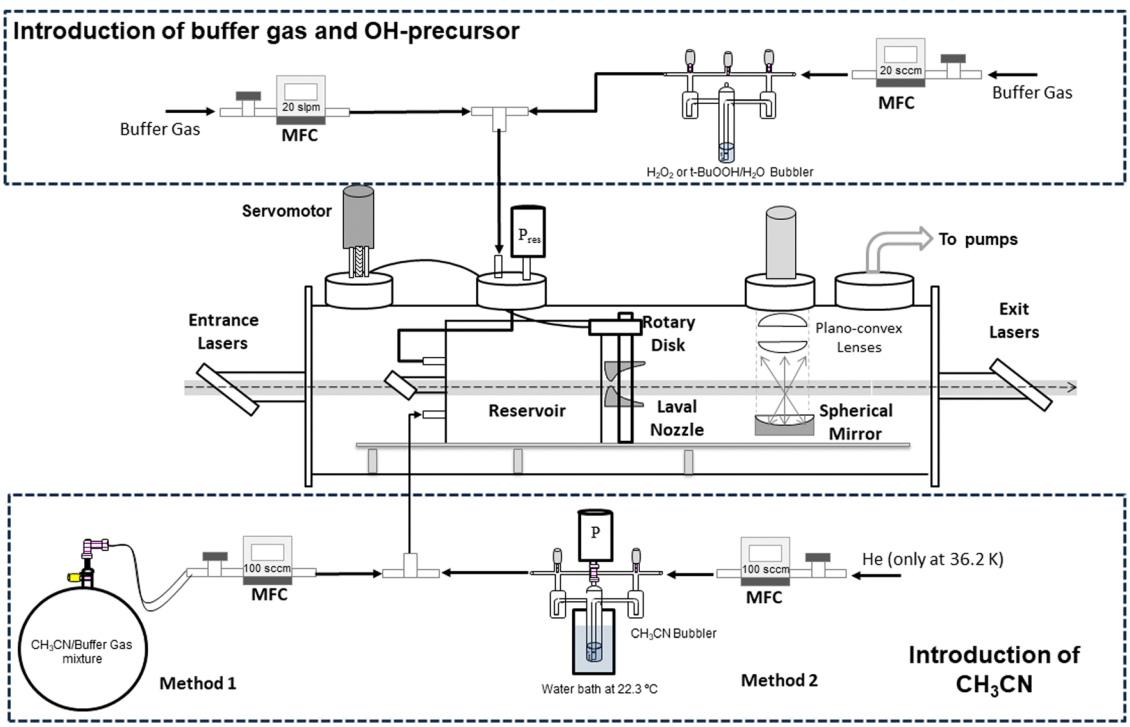

Scheme 1 Experimental set-up scheme including both methods to introduce CH_3CN into the reservoir. MFC: mass flow controller.

where $k(T)$ is the second-order rate coefficient at each temperature and gas density obtained from the slope of the $k' - k'_0$ *vs.* $[CH_3CN]$ plots. Reliable knowledge of $[CH_3CN]$ in the jet is essential to obtain accurate $k(T)$ at each temperature. These concentrations were determined from flow rate or vapor pressure measurements (see ESI†), according to the way CH_3CN is introduced in the reservoir. As shown in Fig. S2 (ESI†), $[CH_3CN]$ determined by both methods yield $k(T)$ at 36.2 K in excellent agreement.

This linear relationship is not accomplished at high $[CH_3CN]$ and the bimolecular plots display a curvature. The observed downward curvature is associated with the dimerization process of CH_3CN, as previously reported for other OH-reactions with COMs (Fig. S2, ESI†).[54–60,62,63,68–70] As can be seen in Fig. S3 (ESI†), the $(CH_3CN)_2$ dimer formation is especially enhanced at low temperatures. Then, the onset of such a dimerization, *i.e.*, $[CH_3CN]$ from which the bimolecular plots are not linear, increases with temperature for a total gas density of the same order of magnitude 10^{17} cm^{-3} (*e.g.* $[CH_3CN]$ = 1.30×10^{14} cm^{-3} at 21.7 K, 1.96×10^{14} cm^{-3} at 76.0 K and 5.30×10^{14} cm^{-3} at 135.0 K). At $T > 140$ K, $k' - k'_0$ *vs.* $[CH_3CN]$ plots are linear in the entire explored $[CH_3CN]$ range, even reaching 1% of the total gas density. Acetonitrile concentration was not increased beyond 1% of the total gas density since it may affect the uniformity of the flow and the jet temperature. In Table 3, $[CH_3CN]$ range within which eqn (E1) is valid are listed for every temperature and gas density. Four examples of the $k' - k'_0$ *vs.* $[CH_3CN]$ plots are shown in Fig. 1 at selected temperatures. As shown, the slope of these plots increases when the temperature decreases, implying that the OH-reactivity of CH_3CN is enhanced at lower temperatures.

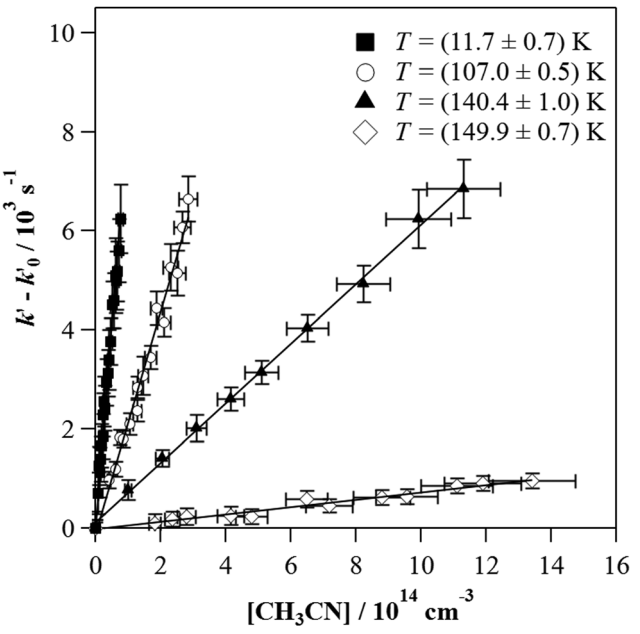

Fig. 1 Examples of $k' - k'_0$ *versus* $[CH_3CN]$ plots at four different temperature conditions. Uncertainties in $[CH_3CN]$ are cautiously considered as ±10% and uncertainties in $k' - k'_0$ are the standard deviation obtained from the analysis of the I_{LIF} decays.

2.2. Chemicals

Buffer gases (He, N_2, and Ar), all of them with 99.999% purity (Nippon Gases Europe), were used as supplied. Liquid acetonitrile (≥99.9%, Sigma-Aldrich) was degassed by repeated freeze-pump-thaw cycles prior to use for the experiments in which the storage bulb was used. The aqueous solution of hydrogen peroxide (50% w/w, Sharlab) was preconcentrated as previously reported,[66] whereas the *t*-BuOOH solution (70%, Sigma-Aldrich) was used directly without pre-concentration, because its vapour pressure is higher than that of H_2O. When no use, both precursor bubblers were stored in a refrigerator at 2 °C to prevent from thermal decomposition.

3. Computational methodology

All geometry optimizations were performed by the M08-HX Density Functional Theory (DFT) method[71] with the MG3S basis set,[72] as for the recently studied OH + CH_3NH_2 reaction.[68] All zero-point energies (ZPEs) were scaled by the recommended factor of 0.973.[73] The two computed reactions are the hydrogen abstraction from the methyl group by the OH radical (reaction (1a)) and the OH-addition to the C of cyano group (reaction (1b)). It is worth noting that reaction (1a) is part of a much larger reaction network recently studied by some of us.[74] The OH-addition to the nitrogen atom, as well as other 4 additional channels previously investigated by Tian *et al.*[51] have very high barriers and are not competitive with reactions (1a) and (1b).

Additional geometry optimizations were also carried out at ωB97X-D[75] with the def2-TZVP basis set.[76] All ZPEs were scaled by the recommended factor of 0.975.[73] The geometries obtained by both electronic structure levels, that is, M08-HX/MG3S and ωB97X-D/def-2TZVP, were employed as input for the CCSD(T)-F12/cc-pVTZ-F12 single-point calculations[77,78] to compare the result of both functionals on an accurate and common ground.

The thermal rate coefficients were evaluated employing the competitive canonical unified theory (CCUS). In this formalism, the rate coefficient for each reaction channel, k_i^{CCUS} (where i = 1a or 1b), is given by eqn (E2),[79]

$$k_i^{CCUS} = k^{CCUS}\alpha_i \quad \text{(E2)}$$

$$k^{CCUS} = \left(\frac{1}{k_a} + \frac{1}{k_1}\right)^{-1} \quad \text{(E3)}$$

where k_a is the rate coefficient for the association reaction and $k_1 = k_{1a} + k_{1b}$ is the total rate coefficient for the OH + CH_3CN reaction calculated as the forward flux from reactants through transition states TS1a (H-abstraction) and TS1b (OH-addition). The ratio between the individual rate coefficients for the transition state passage through k_i and the total rate coefficient k_1 is given by α_i. Because the association reaction is the same for both competitive reactions, the products branching ratio in percentage is given by $100 \cdot \alpha_i$.

The rate coefficient for the association reaction is given by the following expression:[80]

$$k_a = C\mu^{-1/2}(d_{OH}d_{CH_3CN})^{2/3}T^{-1/6} \quad \text{(E4)}$$

where T is the temperature, $C = 1.83 \times 10^{-9}$ is a constant that provides the rate coefficient in $cm^3\ s^{-1}$, μ is the reduced mass (in uma), and $d_{CH_3CN} = 4.02$ D and $d_{OH} = 1.66$ D are the dipole moments of acetonitrile and the OH radical, respectively.

The rate coefficients k_i were calculated employing canonical variational transition state theory with small-curvature tunnelling corrections (CVT/SCT),[81] according to the following equation:

$$k_i^{CVT/SCT} = \Gamma_i^{CVT}\kappa_i^{CVT/SCT}k_i^{TST} \quad \text{(E5)}$$

where k_i^{TST} is the conventional transition state theory (TST) rate coefficient, Γ_i^{CVT} is the variational coefficient that accounts for recrossing ($0 \leq \Gamma_i^{CVT} \leq 1$), and $\kappa_i^{CVT/SCT}$ is the tunnelling transmission coefficient ($\kappa_i^{CVT/SCT} \geq 1$) calculated within the SCT approximation. The evaluation of these two parameters requires the calculation of the minimum energy path (MEP), which was evaluated using the Page-McIver algorithm in mass-scaled coordinates.[82] The MEP for the H-abstraction and OH-addition reactions was followed employing a step size of 0.005 Bohr and Hessian calculations every ten steps. In the case of the reaction through TS1b, we corrected the energies along the MEP to match the coupled-cluster (CC) energy by employing the interpolated single-point energies algorithm.[83] The CVT/SCT calculations were performed with Pilgrim.[84]

The CCUS prescription allows calculating the thermal rate coefficients in the low-pressure (LPL) and high-pressure (HPL) limits. The only difference between the two regimes is that in the LPL the lowest energy for tunnelling is the energy of reactants plus its ZPE, whereas in the HPL the lowest energy that allows tunnelling is the energy of the pre-reactive complex plus its ZPE. For the latter, it is assumed that the collisions with other molecules will stabilize the complex, a situation that cannot occur at very low pressures. Therefore, the only factor affected by pressure in eqn (E5) is the tunnelling transmission coefficient (see Section 4.2).

4. Results and discussion

4.1. Experimental kinetic study

The individual rate coefficients $k(T)$ determined in this work are listed in Table 3 as a function of the OH-precursor (H_2O_2 or *t*-BuOOH), gas density (n), and temperature. As it can be seen in the examples depicted in Fig. 2, no influence of the OH-precursor on $k(T)$ was observed. Thus, in Table 3 the weighted average of $k(T)$ obtained using both precursors is given in bold.

4.1.1. Pressure dependence of $k(T)$. The pressure dependence study of $k(T)$ was carried out for some specific temperatures around 22 K (He as bath gas), 50 K (He, N_2, or Ar as bath gas), and 106 K (N_2 or Ar as bath gas). The total gas density was explored in the range of $(1.50–44.4) \times 10^{16}$ cm^{-3}. n was varied around 5 times at ~22 K, 30 times at ~50 K, and 3 times at ~106 K. As shown in Fig. 3, no pressure dependence of $k(T)$ has been observed at around 22 K, 50 K and 106 K, within the error bars, over the investigated range. This is in agreement with the observations of Sleiman *et al.*[86] for the reaction of CH_3CN with CN radicals at 23 K (He as bath gas). These authors reported a strong dependence of the rate coefficient for the CN-reaction at 52 K and 132 K in Ar. The p-dependence was attributed by these authors as evidence of the adduct formation by association of the reactants (CN and CH_3CN). Even though the gas density range investigated by Sleiman *et al.*[86] is higher ($n = (3.48–82.1) \times 10^{16}$ cm^{-3}) than ours, if a pressure dependence of $k(T)$ for reaction (1) prevails it would have been observed at the concentration level used in the present work.

4.1.2. Temperature dependence of $k(T)$. As shown in Table 3, $k(T)$ increases when temperature decreases, resulting in an acceleration of the reaction of CH_3CN towards OH radicals of around 3800 times at 11.7 K and 10 times at 177.5 K with respect to $k(300\ K) = 2.2 \times 10^{-14}$ $cm^3\ s^{-1}$.[87] The value of $k(177.5\ K)$ reported here (2×10^{-13} $cm^3\ s^{-1}$) is an upper limit, since almost no change in k' with respect to k'_0 was observed in the timescale of the experiment and within the $[CH_3CN]$ range used. This upper limit of k was estimated as explained by Douglas *et al.*,[85] *i.e.*, as twice the uncertainty in k' at the maximum CH_3CN concentration, $[CH_3CN]_{max}$, used in the experiment, divided by that $[CH_3CN]_{max}$. In Fig. 4, the log–log plot of average $k(T)$ from Table 3 *versus* T is presented between 11.7 K and 177.5 K. Clearly, two distinct regions in the plot were observed. Between 135.0 K and 177.5 K, an abrupt decrease of $k(T)$ of a factor of around 90 was observed. In this steep region, the expression of $k(T)$ provided by eqn (E6), where the estimated $k(177.5\ K)$ is excluded, is presented as the blue line in Fig. 4.

$$k(135.0–149.9\ K) = (1.50 \pm 1.48) \times 10^{-20}\left(\frac{T}{300\ K}\right)^{-(26.4\pm1.5)} cm^3\ s^{-1} \quad \text{(E6)}$$

Nevertheless, this expression can be used to extrapolate $k(177.5\ K)$. The extrapolated rate coefficient at 177.5 K is 1.56×10^{-14} $cm^3\ s^{-1}$ (empty black circle in Fig. 4), which is a reasonable value if it is compared with $k(300\ K) = 2.2 \times 10^{-14}$ $cm^3\ s^{-1}$.[87] In contrast, the observed increase of $k(T)$ between 135.0 K and 11.7 K is milder (around 5 times) than that between 135.0 and 149.9 K. The temperature dependence of $k(T)$ in the 11.7–135 K region is well described by eqn (E7) – depicted as the red line in Fig. 4.

$$k(11.7–135.0\ K) = (1.50 \pm 0.12) \times 10^{-11}\left(\frac{T}{300\ K}\right)^{-(0.53\pm0.03)} cm^3\ s^{-1} \quad \text{(E7)}$$

4.2. Computational study

4.2.1. Energetics. The energy of the M08-HX and ωB97X-D stationary points is compared in Table 4 to that of the CCSD(T)-F12 single point calculations with the cc-pVTZ-F12 basis set performed over the M08-HX and ωB97X-D optimized geometries. The DFT energies are substantially different in the two methods and the stability of the two transition states is

Table 3 Summary of the experimental conditions employed in this work, individual $k(T)$ as a function of the gas density (n) and average $k(T)$ (in bold) as a function of temperature[a]

$\approx T$/K	T/K	$n/10^{16}$ cm^{-3}	[CH$_3$CN]/10^{13} cm^{-3}	$k(T)/10^{-11}$ cm^3 s^{-1}
12	11.7 ± 0.7	6.88 ± 0.62	0.76–7.81	8.18 ± 0.85[b]
			1.35–6.15	8.45 ± 0.92[c]
				8.25 ± 0.89
22	21.1 ± 0.6	3.37 ± 0.15	0.87–8.93	7.03 ± 0.86[b]
			0.87–8.89	5.89 ± 0.62[c]
				6.05 ± 1.28
	21.7 ± 1.4	16.65 ± 1.61	1.63–12.7	**6.17 ± 0.71**[b]
36	36.2 ± 1.2	17.73 ± 0.86	2.00–14.5	5.27 ± 0.57[b]
			1.37–15.0	4.91 ± 0.57[c]
				5.14 ± 0.71
50	50.5 ± 1.6	1.50 ± 0.12	1.94–12.5	4.04 ± 0.50[b]
			1.19–8.82	4.29 ± 0.46[c]
				4.23 ± 0.52
	49.9 ± 1.8	3.67 ± 0.32	1.12–9.99	4.33 ± 0.52[b]
			1.12–10.1	3.91 ± 0.57[c]
				4.18 ± 0.71
	52.1 ± 0.5	19.52 ± 0.28	0.83–11.7	4.07 ± 0.42[b]
			0.92–8.08	4.00 ± 0.61[c]
				4.07 ± 0.41
76	76.0 ± 0.8	14.96 ± 0.34	2.19–15.8	**2.70 ± 0.37**[b]
106	106.0 ± 0.6	14.02 ± 0.11	1.26–8.58	2.52 ± 0.38[b]
			0.79–6.52	2.70 ± 0.35[c]
				2.63 ± 0.36
	107.0 ± 0.5	4.90 ± 0.06	4.11–30.1	2.20 ± 0.23[b]
			4.55–14.8	2.28 ± 0.33[c]
				2.21 ± 0.23
135	135.0 ± 0.8	29.45 ± 0.45	6.19–45.4	**1.82 ± 0.20**[b]
	136.1 ± 0.8	24.92 ± 0.35	8.47–63.9	**1.40 ± 0.17**[b]
140	140.4 ± 1.0	21.68 ± 0.40	10.1–113	**0.60 ± 0.06**[b]
	143.3 ± 0.6	17.02 ± 0.17	13.4–166	**0.32 ± 0.04**[b]
150	149.9 ± 0.7	10.69 ± 0.12	18.1–134	**0.07 ± 0.01**[b]
177	177.5 ± 1.2	6.71 ± 0.11	22.8–67.1	**<0.02**[bd]

[a] Uncertainties in $k(T)$ account for statistical ($\pm 2\sigma$) and 10% systematic errors. In n the indicated errors result from the aerodynamic fluctuations in the flow ($\pm 1\sigma$). [b] H_2O_2 as OH-precursor. [c] t-BuOOH as OH-precursor. [d] Upper limit calculated as Douglas *et al.*[85]

reversed when the ZPE is included. However, CCSD(T)-F12 over the DFT geometries produces very similar results, in particular, the CCSD(T)-F12/M08-HX predict that TS1a is 4.51 kcal mol^{-1} above TSb, and 4.65 kcal mol^{-1} when considering CCSD(T)-F12/ωB97X-D calculations. This indicates that both DFT methods supply similar geometries for the stationary points. The potential barrier heights are also in relatively good agreement with the CCSD(T)-F12//B3LYP/6-311++G(3df,3pd) calculations carried out by Alihosseini *et al.*[52] who reported barriers of 5.30 and 1.36 kcal mol^{-1} for TSa and TSb, respectively, with a difference between barriers of 3.94 kcal mol^{-1}.

The difference between the two transition states is reduced to 1.22 and 1.23 kcal mol^{-1} for CCSD(T)-F12/M08-HX and CCSD(T)-F12/ωB97X-D, respectively. These values are in good agreement with the results obtained by Galano,[50] where TS1a is above TS1b by 1.00 kcal mol^{-1}. Of the two DFT methods reported here, M08-HX is the most similar to the coupled-cluster calculations. Additionally, it does not revert the stability of the two transition states, as is the case of the coupled-cluster calculations. Therefore, hereafter all thermal rate coefficient calculations will involve M08-HX calculations of the MEP and additional single-point energy corrections for reaction (1b), to correct the difference between this DFT method and the coupled-cluster calculations. Fig. 5 plots a schematic reaction network of the CCSD(T)-F12/M08-HX ZPE-corrected level regarding reactants, which is the basic scheme for further dynamics calculations.

The pre-reactive complex (C1) and the transition states that correspond to reactions (1a) and (1b) obtained at M08-HX/MG3S are depicted in Fig. 6. It can be observed that the C1 complex can easily react through both transition states.

4.2.2. Computed rate coefficients. The calculated rate coefficient for the association reaction k_a decreases slightly with temperature and it presents a value of 1.28×10^{-9} cm^3 s^{-1} at

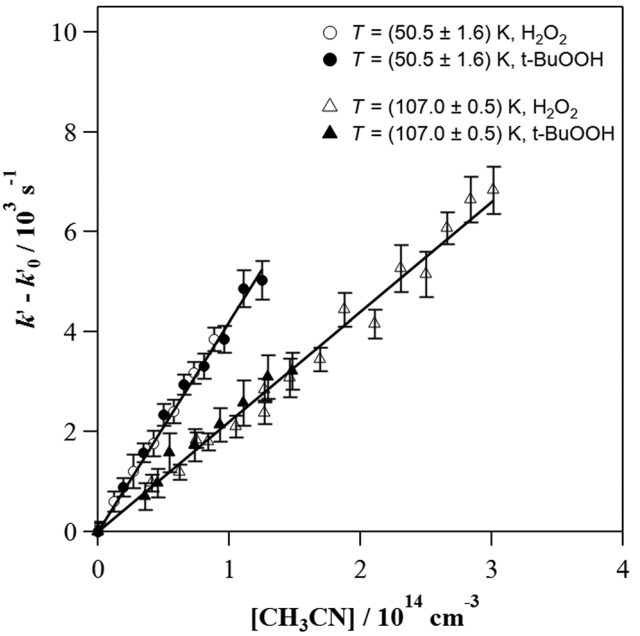

Fig. 2 Examples of the bimolecular plots at 50.5 and 107.0 K using two OH-precursors.

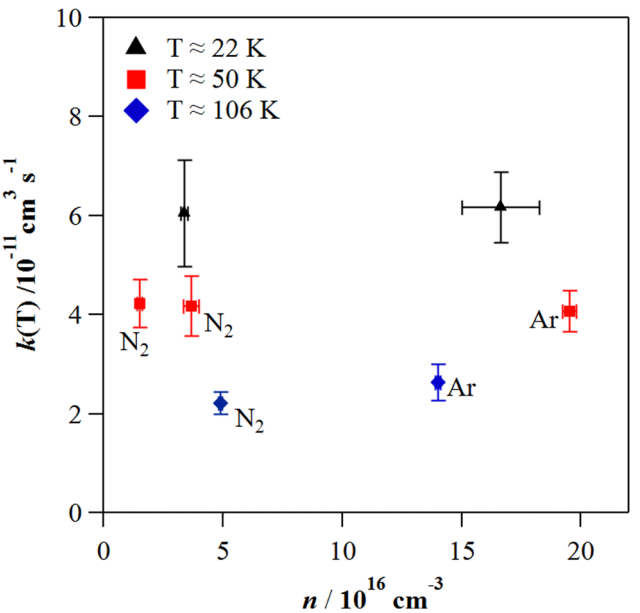

Fig. 3 Dependence of $k(T)$ on the jet gas density (n) at *ca.* 22, 50, and 106 K. Black triangles correspond to experiments at 22 K in He, while at 50 and 106 K the bath gas is indicated next to each point. Error bars in $k(T)$ are statistical ($\pm 2\sigma$) and 10% systematic errors and in n are only statistical ($\pm\sigma$).

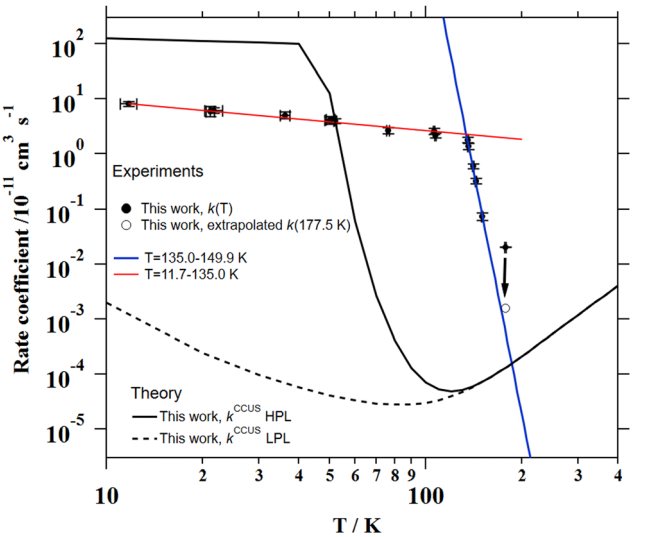

Fig. 4 Experimental and theoretical temperature dependence of the rate coefficient for the CH_3CN + OH reaction. Red and blue lines represent the resulting fit to $k(T) = A\ (T/300\ \mathrm{K})^n$ in the stated temperature range. Solid and dashed black curves are the computed HPL and LPL rate coefficients.

T = 10 K, and a value of 9.75×10^{-10} cm^3 s^{-1} at T = 50 K. In Table 5, variational and tunnelling transmission coefficients are presented for selected temperatures between 50 and 300 K. A full account of these parameters and the thermal rate coefficients k_{1a} and k_{1b} is given in the ESI.†

Tunnelling effects are more important for the H-abstraction than for the OH-addition reaction. This is expected as the hydrogen atom is a light particle, whereas the OH-addition involves heavy-atom tunnelling.[88] However, variational effects are also more relevant in the H-abstraction reaction, so the result of multiplying the variational coefficient by the tunnelling coefficient favours the addition reaction. Moreover, the potential barrier is higher for the H-abstraction reaction and therefore the OH-addition reaction dominates between 10 and 300 K. In fact, it contributes 100% at 10 K and 87% at 300 K.

The variational effect in the H-abstraction shows the magnitude of recrossing in the reaction. In CVT/SCT, this effect is calculated by finding the maximum of the Gibbs free energy along the reaction coordinate s of the MEP (negative in the reactant site, positive in the products site and zero at the transition state), which for the abstraction reaction is located at s = −0.267 Bohr at 0 K and at s = −0.250 Bohr at 400 K. Variational effects are due to the increasing value of the ZPE as we head toward reactants; it is 31.51 kcal mol^{-1} at the transition state and 33.17 kcal mol^{-1} at s = −0.250 Bohr. This ZPE variation displaces the maximum of the free energy towards the reactants site.

For the evaluation of the normal-mode frequencies along the MEP, we have employed redundant internal coordinates, because it is well-known that an accurate evaluation of the ZPE along the reaction path requires the use of internal coordinates. They provide a more physical description of the normal-mode frequencies than the Cartesian coordinates (notice that the calculated normal mode frequencies in non-stationary points depend on the system of coordinates).[89] Theoretical methods based on conventional TST that incorporate tunnelling effects (for instance, through the Eckart barrier), completely ignore the recrossing, which in this case has the effect of reversing the contribution of the two channels to the branching ratios.

We have also included torsional anharmonicity in the transition state structures applying the same protocol as for the

Table 4 Relative energies (ΔE) and ZPE-corrected energies (ΔH_0°) with respect to reactants of the complex (C), transition states (TS), and products (P) for reactions (1a) and (1b). Optimizations at the M08-HX and ωB97X-D levels and single-point calculations at the CCSD(T)-F12 level. Energies in kcal mol^{-1}

	$\Delta E_{M08/\omega B97}$	$\Delta E_{CC(M08/\omega B97)}$	$\Delta H^\circ_{0,M08/\omega B97}$	$\Delta H^\circ_{0,CC(M08/\omega B97)}$
Reactants	0.00/0.00	0.00/0.00	0.00/0.00	0.00/0.00
C1	−5.20/−4.04	−3.88/−4.03	−4.24/−3.30	−2.90/−3.09
TS1a	5.67/3.12	5.71/5.77	4.09/1.42	4.13/4.05
P1a	−21.21/20.27	−21.36/−21.40	−21.91/−21.10	−22.06/−22.23
TS1b	2.18/−0.03	1.20/1.12	3.89/1.69	2.91/2.82
P1b	−28.98/−32.31	−28.46/−28.42	−24.90/−27.90	−24.38/−24.01

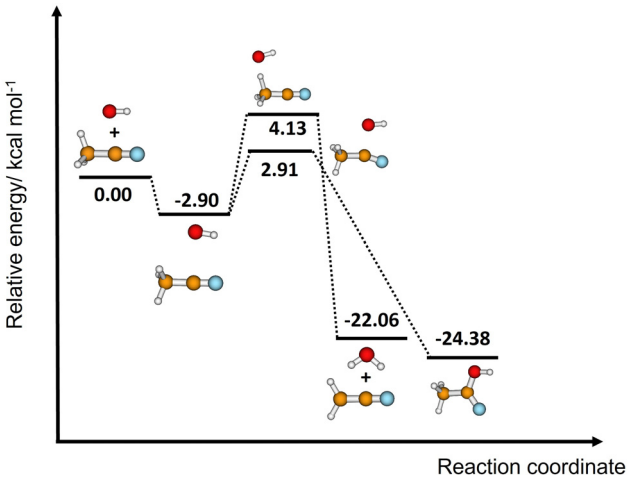

Fig. 5 Schematic ZPE-corrected energy diagram at the CCSD(T)-F12/M08-HX level of theory for reactions (1a) and (1b). See the last column of Table 4.

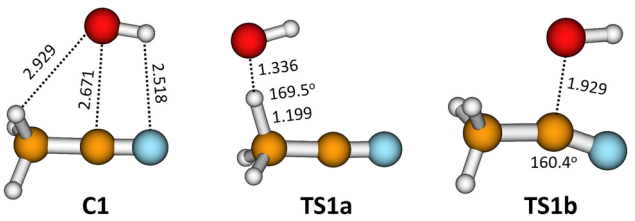

Fig. 6 Pre-reactive complex (C1), TS1a, and TS1b structures with some selected distances (in Å) and bond angles (in degrees). Geometries optimized at the M08/MG3S level.

OH + methylamine system.[68] In the case of TS1a, the torsional anharmonicity contains the rotation of the OH about the methyl group (with a harmonic frequency ω = 144.2 cm^{-1}). For TS1b, there are two rotors, the internal rotation of the OH (with ω = 221.2 cm^{-1}) and methyl (with ω = 140.8 cm^{-1}) groups. For the two transition states, the treatment of these motions, as one-dimensional hindered rotors, instead of harmonic oscillators has a modest effect in the rate coefficients. The ratio between the anharmonic and harmonic partition functions is always smaller than 2 between 50 and 400 K (see the ESI†).

The total CCUS rate coefficients are plotted in Fig. 4 and summarized in Table 6 for selected temperatures. At the LPL, $k_a \gg k_1$ and the rate-determining reaction is always k_1, so this rate coefficient and k^{CCUS} coincide. Above T = 150 K the thermal rate coefficients evaluated at the two pressure limits coincide, this is because at this temperature and above the molecules populate the same levels with independence of the depth of the lowest energy level. In other words, the pre-reactive complex is irrelevant for the course of the reaction. However, below T = 150 K the HPL rate coefficients start to increase fast and at $T \sim$ 40 K k_{HPL} becomes larger than the association rate coefficient, being k_a the rate-determining reaction. Although the agreement between theory and experiment obtained in this work is not perfect, the HPL results capture the wild variation of the rate coefficients with an astonishing increase of about four orders of magnitude in an interval of less than 100 K.

4.3. Comparison with previous studies

4.3.1. Experimental OH-reactivity trend towards CH_3X molecules (X = –CN, –OH, –NH_2, –CHO, CH_2OH, –C(O)CH_3...). The OH-reactivity and its temperature dependence at very low temperatures can be analysed for CH_3X molecules, such as CH_3CN, CH_3OH, CH_3NH_2, CH_3CHO, or CH_3CH_2OH. As it can be seen in Fig. 7, the T-dependence of $k(T)$ for the CH_3CN + OH reaction presents a "pipe-type" shape already observed for the CH_3OH + OH[55,90,91] and CH_3CH_2OH + OH[54,92] reactions. In the low temperature regime, these "pipe-type" shape plots are characterized by a drastic change in the OH-reactivity at a certain temperature followed by a slighter increase in $k(T)$ when the temperature approaches 10 K. The change in the trend for the T-dependence of $k(T)$ appears between 177.5 and 250 K for the CH_3CN + OH reaction, while the minimum $k(T)$ was observed at ∼200 K for the reaction of OH with CH_3OH[90] or CH_3CH_2OH. For the $CH_3C(O)CH_3$ + OH reaction, the expected minimum $k(T)$ must lie somewhere between 300 K and 146 K.[93] In contrast, for the CH_3NH_2 + OH[68] and CH_3CHO + OH[56] reactions, a "hammock-type" shape was observed, *i.e.* once the change in trend in the T-dependence $k(T)$ is produced, it continuously increases at low temperatures. For CH_3CHO, the minimum $k(T)$ was observed at ∼500 K.[56]

4.3.2. Experimental CH_3CN + R reactions (R = OH, CN, C_2H, $C(^3P)$ or $O(^1D)$). When comparing the OH-reactivity towards CH_3CN, with that of other radicals, such as CN, C_2H, $C(^3P)$, or $O(^1D)$, we find scarce kinetic information. Particularly interesting is the comparison between OH and CN reactions,[86] where a similar behaviour was observed in the low temperature regime. For the CH_3CN + CN reaction,[86] a "pipe-type" shape was also reported with an expected minimum $k(T)$ between 168 and 258 K. The interpretation of the increase in $k(T)$ when

Table 5 Variational and tunnelling transmission coefficients, and TST thermal rate coefficients (in $cm^3\ s^{-1}$) at selected temperatures between 50 and 300 K

T (K)	Γ_{1a}^{CVT}	$\kappa_{1a,LPL}^{CVT/SCT}$	$\kappa_{1a,HPL}^{CVT/SCT}$	k_{1a}^{TST}	Γ_{1b}^{CVT}	$\kappa_{1b,LPL}^{CVT/SCT}$	$\kappa_{1b,HPL}^{CVT/SCT}$	k_{1b}^{TST}
50	1.22×10^{-5}	5.90×10^{12}	1.60×10^{14}	1.10×10^{-29}	0.740	4.73×10^{8}	1.67×10^{14}	1.18×10^{-24}
100	3.83×10^{-3}	1.13×10^{4}	1.48×10^{4}	4.32×10^{-21}	0.838	4.13×10^{2}	9.64×10^{2}	8.70×10^{-19}
150	2.63×10^{-2}	56.5	57.8	3.31×10^{-18}	0.854	11.4	11.4	7.33×10^{-17}
200	6.93×10^{-2}	8.87	8.89	9.91×10^{-17}	0.852	3.58	3.58	6.93×10^{-16}
300	0.181	2.56	2.56	3.50×10^{-15}	0.838	1.71	1.71	7.25×10^{-15}

decreasing temperature, given by Sleiman *et al.*[86] for the CN-reaction, is based on the increase in the probability of stabilization of the pre-reactive complex. The abrupt decrease in the rate coefficient observed at 168 K was related to the lack of stability of the $CH_3CN\cdots CN$ complex at higher temperatures since it decomposes on the same timescale as collision induced vibrational energy relaxation. As shown in Fig. 7, OH and CN radicals surprisingly present a similar reactivity towards CH_3CN and an analogous trend in temperature dependence.

For the C_2H + CH_3CN reaction (T = 165–360 K),[94,95] the combination of the kinetic data from Nizamov and Leone[94] and Hoobler and Leone[95] yields the following Arrhenius expression $(1.80 \pm 0.35) \times 10^{-11} \exp(-(766 \pm 38)/T)\ cm^3\ s^{-1}$. An increase of almost one order of magnitude between 165 K and 296 K was reported by Nizamov and Leone.[94] However, the complete picture of the temperature dependence of the rate coefficient for the C_2H + CH_3CN reaction cannot be seen at very low temperatures since no kinetic measurements were performed below 165 K.

For the $C(^3P)$ + CH_3CN reaction (T = 50–296 K), even though it is very fast, Hickson *et al.*[96] reported no temperature dependence of $k(T)$ in that temperature range. The same group also investigated the $O(^1D)$ + CH_3CN reaction at 75, 127 and 296 K,[97] obtaining rate coefficients close to the collision limit ($(2.4–3.7) \times 10^{-10}\ cm^3\ s^{-1}$) with a tendency to increase below 127 K. Nonetheless, the authors recommend using a temperature independent value of $(2.85 \pm 0.70) \times 10^{-10}\ cm^3\ s^{-1}$ in the explored temperature range.

4.3.3. Comparison between experiments and theory. In Fig. 8, the complete picture of the temperature dependence of $k(T)$ between 10 and 3000 K is depicted, which includes both experimental and previous theoretical studies for comparison purposes. As shown in this figure, the LPL rate coefficient reported in this work increases at very low temperatures, but their values are more than three orders of magnitude smaller than the present experimental results. In other words, these are closer to the HPL than to the LPL. In fact, the experimental results follow the same trend as those of the CH_3CN + CN reaction[86] (see Fig. 7). At very low temperatures (below 50 K, in the theory, and below 140 K in the experiment) the CH_3CN + OH reaction is controlled by the association reaction, with a very mild-decreasing temperature dependence. After that, there is a very rapid decrease in the rate coefficient with increasing temperature, which is mainly due to tunnelling at energies below the energy of reactants. We may consider that the dynamics of this region is controlled by tunnelling and by the depth of the pre-reactive complex. Finally, above 250 K, the temperature dependence of the rate coefficient k^{CCUS} is positive, and the reaction is dominated by tunnelling above reactants and by overbarrier dynamics. This is consistent with previously reported experimental and theoretical temperature dependencies of $k(T)$, which reveal an Arrhenius-like behaviour, with $k(T)$ decreasing while temperature is lowered,[40,41,44,45,47,51,53] except for Alihosseini *et al.*[52] who predicted a non-Arrhenius behaviour. Moreover, these authors overestimated the rate coefficients by several orders of magnitude in the experimental temperature range. Tian *et al.*[51] also overestimated $k(T)$ in the entire T-range. Note that the extrapolated rate coefficients from the work of Li and Wang[53] and Tian *et al.*[51] down to 150 K show that the crossing temperature with our extrapolated low-temperature data using eqn (E6) is 183 K (see Fig. 4). Therefore, the minimum $k(T)$ is expected to lie around 180 K.

As mentioned in the Introduction, several studies reported branching ratios for channels (1a) and (1b) at room temperature. More particularly, some evidence of the existence of the OH-addition route was pointed out as briefly discussed in the Introduction section and summarized in Tables 2 and 3.

Experimentally, Hynes and Wyne[45] claimed that the OH-addition channel (1b) accounted for about 50% of the total reaction process. This is, however, an indirect conclusion based

Table 6 Low- and high-pressure limit CCUS rate coefficients (in $cm^3\ s^{-1}$) at selected temperatures between 10 and 400 K

	k_{1a}^{CCUS}	k_{1b}^{CCUS}	k^{CCUS}	k_{1a}^{CCUS}	k_{1b}^{CCUS}	k^{CCUS}
T (K)	LPL			HPL		
10	1.083×10^{-37}	2.003×10^{-14}	2.003×10^{-14}	1.123×10^{-16}	1.275×10^{-9}	1.275×10^{-9}
50	7.89×10^{-22}	4.102×10^{-16}	4.102×10^{-16}	2.241×10^{-20}	1.266×10^{-10}	1.266×10^{-10}
100	1.867×10^{-19}	3.013×10^{-16}	3.015×10^{-16}	2.440×10^{-19}	7.032×10^{-16}	7.034×10^{-16}
150	4.192×10^{-18}	7.155×10^{-16}	7.204×10^{-16}	5.024×10^{-18}	7.161×10^{-16}	7.211×10^{-16}
200	6.063×10^{-17}	2.068×10^{-15}	2.129×10^{-15}	6.079×10^{-17}	2.068×10^{-15}	2.129×10^{-15}
300	1.600×10^{-15}	1.030×10^{-14}	1.190×10^{-14}	1.601×10^{-15}	1.030×10^{-14}	1.190×10^{-14}
400	1.152×10^{-14}	2.871×10^{-14}	4.022×10^{-14}	1.152×10^{-14}	2.871×10^{-14}	4.022×10^{-14}

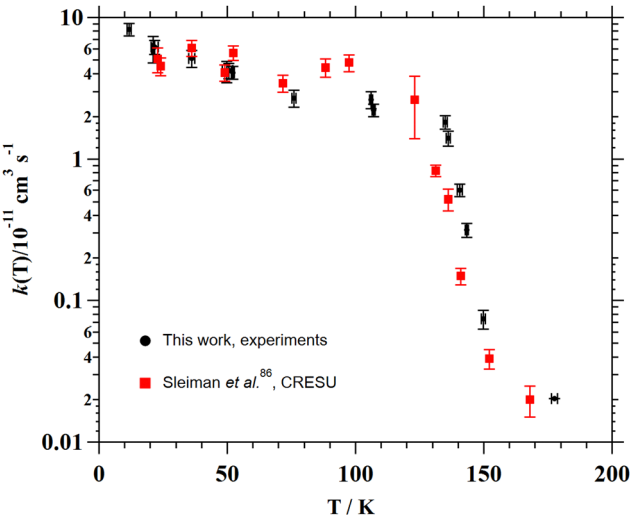

Fig. 7 Comparison between the temperature dependence of $k(T)$ for the OH- and CN-reaction of CH_3CN below 200 K.

on the observation that, in their reactor, the OH temporal decay was smaller in the presence of molecular oxygen than in its absence. The authors analysed this finding by considering that OH regeneration was occurring in their experiment. This was also observed for the OH + CD_3CN reaction in the presence of O_2 and they deduced that the OH-addition channel was necessarily open because the other potential product (CD_2CN radical) could obviously not release OH by reaction with O_2. By simulating their various OH temporal decays they estimated that the two possible channels for reaction (1) have essentially similar rate coefficients. Later, Tyndall *et al.*[46] investigated the title reaction in a smog chamber filled with synthetic air. Infrared observation of the terminal product HC(O)CN with a yield of (40 ± 20)% led them to conclude that their measurement was consistent with the conclusions brought by Hynes and Wine[45] concerning the possible routes of reaction (1).

From a theoretical point of view, the OH-addition channel was only investigated by Galano[50] who also studied the reaction mechanisms in the presence of O_2. She found that, in atmospheric conditions, reaction (1) will eventually lead to the formation of HC(O)CN in agreement with the smog chamber experiment from Tyndall *et al.*[46] Further, she demonstrated that molecular oxygen could attack the N of $CH_3C(OH)N$ – product from reaction (1b) – generating a hexagonal structure which will eventually release an OH radical agreeing thus with the suggestions of Hynes and Wine.[45] Although Galano[50] did not estimate the branching ratios for reactions (1a) and (1b), based on energetic considerations, she stated that reaction (1) should lead to the formation of both species CH_2CN and $CH_3C(OH)N$ in similar proportions. In the present work, we computed that the OH-addition reaction contributes 87% at 300 K (see ESI†), a temperature for which no pressure dependence is predicted. At lower temperatures, *i.e.* below 150 K, the OH-addition channel becomes the only viable route.

4.4. Astrochemical modelling

Since densities are very small in interstellar molecular clouds (typically 10^4–10^6 cm^{-3}), chemical reactions which are pressure dependent can be of potential interest in their LPL regime only. In a recent study concerning the OH + CH_3OH reaction,[55,98] it has been shown that, at temperatures of typically 10–20 K, the total rate coefficients in the HPL and the LPL regimes were essentially similar. This is not the case for the present reaction according to our theoretical calculations which suggest that experimental measurements below 20 K are closer to the HPL than to the LPL. Hence, to evaluate the impact of the reaction presently studied on the chemical composition of cold dense clouds, where the gas kinetic temperature is as low as 10 K, we carried out chemical modelling calculations assuming the theoretical k_{CCUS} at the LPL (2×10^{-14} cm^3 s^{-1} at 10 K) and that the main channel is the formation of $CH_3C(OH)N$. We adopted typical parameters of cold dense clouds, *i.e.* a H_2 volume density of 2×10^4 cm^{-3}, a visual extinction of 30 mag, and a cosmic-ray ionization rate of 1.3×10^{-17} s^{-1}. We adopted the elemental abundances commonly known as "low-metal" values, in which the abundances of metals, silicon, and sulphur are reduced with respect to the values observed in diffuse clouds.[99] We used the chemical network rate.2012 from the UMIST database.[100] The results of the model show that reaction (1b) does not have any effect on the abundance of CH_3CN. According to the UMIST network, the main reactions of destruction of CH_3CN are those with cations, such as H_3O^+, HCO^+, and C^+. The reaction with OH has a marginal (1%) contribution to the destruction of CH_3CN. Indeed, the reactions with H_3O^+ and HCO^+ are not fully effective in destroying CH_3CN because they produce the protonated form of CH_3CN, which partially gives back CH_3CN when recombining dissociatively

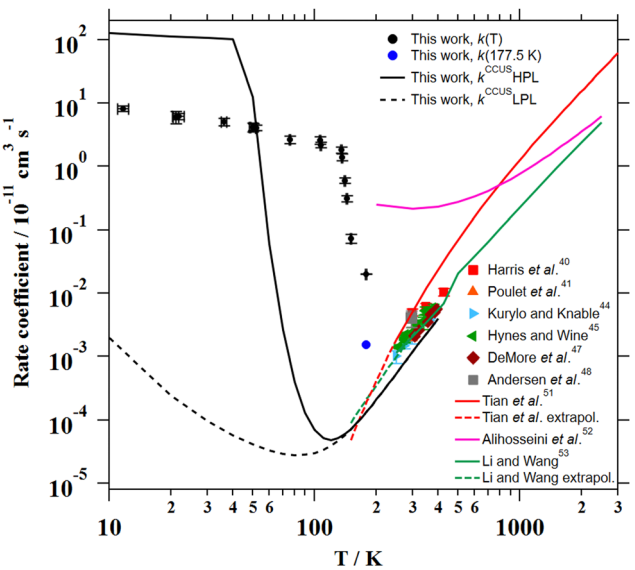

Fig. 8 Experimental and theoretical temperature dependencies of the rate coefficient for the CH_3CN + OH reaction.

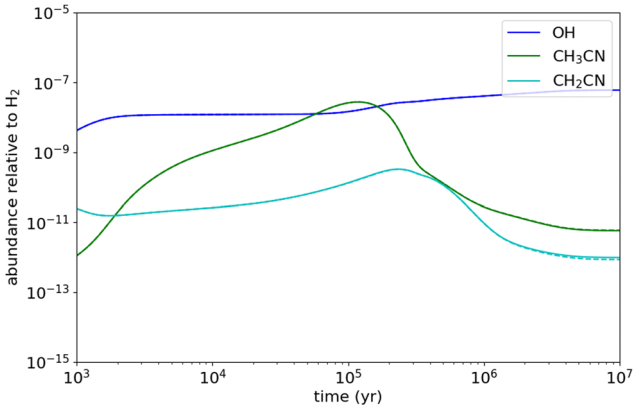

Fig. 9 Abundances relative to H_2 as a function of time calculated with the chemical model when excluding the CH_3CN + OH reaction (dashed lines) and including it (solid lines) with a rate coefficient of 8.25×10^{-11} cm^3 s^{-1}, as measured in this work at 11.7 K.

with electrons. The reaction with C^+ however is an efficient process of removal of CH_3CN. The rate coefficient of this reaction has been measured to be 5.6×10^{-9} cm^3 s^{-1} at 300 K,[101] and it is likely even higher at 10 K, following the usual behaviour of ion-polar reactions.[102]

Even though if we assume the total rate coefficient measured at 11.7 K as a higher limit of the reactivity of CH_3CN, the impact of reaction (1) on the abundance of CH_3CN is very little (see Fig. 9). Furthermore, assuming as well that the CH_2CN radical would be the sole product, the CH_3CN + OH reaction would contribute to its gas-phase formation with around 2%. According to the UMIST network, the main reaction forming CH_2CN is the N + C_2H_3 reaction. Nevertheless, the N + C_2H_3 reaction has been measured to be relatively fast, 7.7×10^{-11} cm^3 s^{-1}, at 298 K, and the main product channel has been inferred to be CH_2CN + H.[103] It is however unknown whether this rate coefficient and product distribution holds also at the very low temperatures of cold dense clouds.

It is desirable to have experimental evidence of the formation of CH_2CN or $CH_3C(OH)CN$ radicals from the CH_3CN + OH reaction at very low temperatures.

5. Conclusions

The present experimental results show that acetonitrile (CH_3CN) reacts very fast with OH radicals in the gas phase at very low temperatures (~10–100 K). Since the temperature behaviour of the rate coefficient varies in the explored experimental range, we provide two analytical expressions using a modified Arrhenius expression, $\left(k(T) = \alpha\left(\frac{T}{300\ \mathrm{K}}\right)^{\beta} \exp\left(-\frac{\gamma}{T}\right)\right.$, with $\alpha = 1.50 \times 10^{-11}$ cm^3 s^{-1}; $\beta = -0.53$ and $\gamma = 0$ K) between 11.7 K and 135 K and $\alpha = 1.5 \times 10^{-20}$ cm^3 s^{-1}; $\beta = -26.4$ and $\gamma = 0$ K between 135 K and 149.9 K, a temperature within which the dependence of the rate coefficient $k(T)$ is extremely fast, changing more than one order of magnitude in only 15 K.

The computational results indicate that below 150 K, the reaction product is $CH_3C(OH)N$ and not CH_2CN. Moreover, the experimental rate coefficients have been found to be pressure independent at 22 K, 50 K and 106 K and appear to be much closer to the calculated high-pressure limit than to the low-pressure regime. Above 150 K, the contribution of the H-abstraction channel begins to increase, reaching 13% at 300 K and 29% at 400 K. It is worthwhile to point out that very efficient heavy-atom tunnelling has been highlighted by the present quantum calculations which is quite unusual.

According to the model (T = 10 K), the impact of the titled reaction on the abundances of CH_3CN appears to be negligible in dark molecular clouds of the ISM (~1% of the total depletion reactions included in UMIST network). Respect to the potential formation of the CH_2CN radical in those environments, even in the most favourable scenario, where this radical could be formed in a 100% yield from the CH_3CN + OH reaction, this route would only contribute around 2% to the current assumed formation routes by UMIST network.

Author contributions

DG and AC performed the experiments and data analysis and wrote the original draft of the paper; EMN and AFR carried out the theoretical calculations; MA and JC run the astrochemical model; BB, AC, and EJ designed and supervised the experiments; EJ got funds for carrying out the present experimental research; all authors contributed to the critical discussion and review of the draft.

Conflicts of interest

There are no conflicts to declare.

Acknowledgements

This work has been supported by the Spanish Ministry of Science and Innovation (MICINN) through CHEMLIFE project (grant PID2020-113936GB-I00), by the regional government of Castilla-La Mancha and the European Regional Development Fund (ERDF) through CINEMOL project (grant SBPLY/19/180501/000052), and by the University of Castilla-La Mancha – UCLM (2022-GRIN-34143) also co-funded by ERDF. This work was partially supported by the Consellería de Cultura, Educación e Ordenación Universitaria (Centro singular de investigación de Galicia acreditación 2019-2022, ED431G 2019/03 and Grupo de referencia competitiva ED431C 2021/40) and ERDF, and the Spanish MICINN through the Grant #PID2019-107307RB-I00. AFR and EMN thank the Centro de Supercomputación de Galicia (CESGA) for the use of their computational facilities. D. González also acknowledges UCLM (Plan Propio de Investigación) for funding his contract during the performance of this investigation. AC is grateful to the University of Rennes for supporting his stay at UCLM under its International Action programme.

References

1 J. Gadhi, A. Lahrouni, J. Legrand and J. Demaison, *J. Chim. Phys.*, 1995, **92**, 1984–1992.
2 Q. Li, D. J. Jacob, R. M. Yantosca, C. L. Heald, H. B. Singh, M. Koike, Y. Zhao, G. W. Sachse and D. G. Streets, *J. Geophys. Res. Atmos.*, 2003, **108**(D21), 8827.
3 J. J. Harrison and P. F. Bernath, *Atmos. Chem. Phys.*, 2013, **13**, 7405–7413.
4 D. Bockelée-Morvan and N. Biver, *Philos. Trans. R. Soc., A*, 2017, **375**, 20160252.
5 B. L. Ulich and E. K. Conklin, *Nature*, 1974, **248**, 121–122.
6 N. Biver, D. Bockelée-Morvan, P. Colom, J. Crovisier, B. Germain, E. Lellouch, J. K. Davies, W. R. F. Dent, R. Moreno, G. Paubert, J. Wink, D. Despois, D. C. Lis, D. Mehringer, D. Benford, M. Gardner, T. G. Phillips, M. Gunnarsson, H. Rickman, A. Winnberg, P. Bergman, L. E. B. Johansson and H. Rauer, *Earth, Moon, Planets*, 1997, **78**, 5–11.
7 A. J. Remijan, S. N. Milam, M. Womack, A. J. Apponi, L. M. Ziurys, S. Wyckoff, M. F. A'Hearn, I. de Pater, J. R. Forster, D. N. Friedel, P. Palmer, L. E. Snyder, J. M. Veal, L. M. Woodney and M. C. H. Wright, *Astrophys. J.*, 2008, **689**, 613–621.
8 J. Geiss, K. Altwegg, H. Balsiger and S. Graf, *Space Sci. Rev.*, 1999, **90**, 253–268.
9 M. Rubin, K. Altwegg, H. Balsiger, J. J. Berthelier, M. R. Combi, J. de Keyser, M. Drozdovskaya, B. Fiethe, S. A. Fuselier, S. Gasc, T. I. Gombosi, N. Hänni, K. C. Hansen, U. Mall, H. Rème, I. R. H. G. Schroeder, M. Schuhmann, T. Sémon, J. H. Waite, S. F. Wampfler and P. Wurz, *Mon. Not. R. Astron. Soc.*, 2019, **489**, 594–607.
10 A. Marten, T. Hidayat, Y. Biraud and R. Moreno, *Icarus*, 2002, **158**, 532–544.
11 V. Vuitton, R. V. Yelle and M. J. McEwan, *Icarus*, 2007, **191**, 722–742.
12 P. M. Solomon, K. B. Jefferts, A. A. Penzias and R. W. Wilson, *Astrophys. J.*, 1971, **168**, L107.
13 V. Thiel, A. Belloche, K. M. Menten, R. T. Garrod and H. S. P. Müller, *Astron. Astrophys.*, 2017, **605**, L6.
14 H. Liszt, M. Gerin, A. Beasley and J. Pety, *Astrophys. J.*, 2018, **856**, 151.
15 M. Araki, S. Takano, N. Kuze, Y. Minami, T. Oyama, K. Kamegai, Y. Sumiyoshi and K. Tsukiyama, *Mon. Not. R. Astron. Soc.*, 2020, **497**, 1521–1535.
16 H. E. Matthews and T. J. Sears, *Astrophys. J.*, 1983, **267**, L53.
17 P. Gratier, J. Pety, V. Guzmán, M. Gerin, J. R. Goicoechea, E. Roueff and A. Faure, *Astron. Astrophys.*, 2013, **557**, 1–19.
18 S. Cuadrado, J. R. Goicoechea, J. Cernicharo, A. Fuente, J. Pety and B. Tercero, *Astron. Astrophys.*, 2017, **603**, A124.
19 M. Guélin and J. Cernicharo, *Astron. Astrophys.*, 1991, **244**, L21–L24.
20 M. Agúndez, J. Cernicharo, G. Quintana-Lacaci, L. V. Prieto, A. Castro-Carrizo, N. Marcelino and M. Guélin, *Astrophys. J.*, 2015, **814**, 143.
21 L. Olmi, R. Cesaroni, R. Neri and C. M. Walmsley, *Astron. Astrophys.*, 1996, **315**, 565–577.
22 A. Remijan, E. C. Sutton, L. E. Snyder, D. N. Friedel, S.-Y. Liu and C.-C. Pei, *Astrophys. J.*, 2004, **606**, 917–928.
23 V. Pankonin, E. Churchwell, C. Watson and J. H. Bieging, *Astrophys. J.*, 2001, **558**, 194–203.
24 S. Mercimek, C. Codella, L. Podio, E. Bianchi, L. Chahine, M. Bouvier, A. López-Sepulcre, R. Neri and C. Ceccarelli, *Astron. Astrophys.*, 2022, **659**, 1–43.
25 K. I. Öberg, V. V. Guzmán, K. Furuya, C. Qi, Y. Aikawa, S. M. Andrews, R. Loomis and D. J. Wilner, *Nature*, 2015, **520**, 198–201.
26 J. B. Bergner, V. G. Guzmán, K. I. Öberg, R. A. Loomis and J. Pegues, *Astrophys. J.*, 2018, **857**, 69.
27 H. G. Arce, J. Santiago-García, J. K. Jørgensen, M. Tafalla and R. Bachiller, *Astrophys. J.*, 2008, **681**, L21–L24.
28 T. Hung, S.-Y. Liu, Y.-N. Su, J. H. He, H.-T. Lee, S. Takahashi and H.-R. Chen, *Astrophys. J.*, 2019, **872**, 61.
29 R. Mauersberger, C. Henkel, C. M. Walmsley, L. J. Sage and T. Wiklind, *Astron. Astrophys.*, 1991, **247**, 307–314.
30 T. Nakajima, S. Takano, K. Kohno, N. Harada and E. Herbst, *Publ. Astron. Soc. Jpn.*, 2018, **70**, 1–36.
31 D. J. Wilner, M. C. H. Wright and R. L. Plambeck, *Astrophys. J.*, 1994, **422**, 642.
32 E. Araya, P. Hofner, S. Kurtz, L. Bronfman and S. DeDeo, *Astrophys. J., Suppl. Ser.*, 2005, **157**, 279–301.
33 C. Codella, M. Benedettini, M. T. Beltrán, F. Gueth, S. Viti, R. Bachiller, M. Tafalla, S. Cabrit, A. Fuente and B. Lefloch, *Astron. Astrophys.*, 2009, **507**, 2005–2008.
34 A. Palau, C. Walsh, Á. Sánchez-Monge, J. M. Girart, R. Cesaroni, I. Jiménez-Serra, A. Fuente, L. A. Zapata and R. Neri, *Mon. Not. R. Astron. Soc.*, 2017, **467**, 2723–2752.
35 L. Giani, C. Ceccarelli, L. Mancini, E. Bianchi, F. Pirani, M. Rosi and N. Balucani, *Mon. Not. R. Astron. Soc.*, 2023, **526**, 4535–4556.
36 K. Acharyya, E. Herbst, R. L. Caravan, R. J. Shannon, M. A. Blitz and D. E. Heard, *Astron. Astrophys.*, 2015, **113**, 2243–2254.
37 S. Cazaux, V. Cobut, M. Marseille, M. Spaans and P. Caselli, *Astron. Astrophys.*, 2010, **522**, A74.
38 J. R. Goicoechea, C. Joblin, A. Contursi, O. Berné, J. Cernicharo, M. Gerin, J. Le Bourlot, E. A. Bergin, T. A. Bell and M. Röllig, *Astron. Astrophys.*, 2011, **530**, L16.
39 H. Linnartz, S. Ioppolo and G. Fedoseev, *Int. Rev. Phys. Chem.*, 2015, **34**, 205–237.
40 G. W. Harris, T. E. Kleindienst and J. N. Pitts, *Chem. Phys. Lett.*, 1981, **80**, 479–483.
41 G. Poulet, G. Laverdet, J. L. Jourdain and G. Le Bras, *J. Phys. Chem.*, 1984, **88**, 6259–6263.
42 B. Fritz, K. Lorenz, W. Steinert and R. Zellner, *Proc. 2nd Eur. Symp. Physico-Chemical Behav. Atmos. Pollut.*, 1982, p. 192.
43 C. Zetzsch, *Bunsekolloquium*, Battelle Institut, Frankfurt, 1983.
44 M. J. Kurylo and G. L. Knable, *J. Phys. Chem.*, 1984, **88**, 3305–3308.
45 A. J. Hynes and P. H. Wine, *J. Phys. Chem.*, 1991, **95**, 1232–1240.

46 G. S. Tyndall, J. J. Orlando, T. J. Wallington and M. D. Hurley, *J. Phys. Chem. A*, 2001, **105**, 5380–5384.
47 W. B. DeMore, *J. Photochem. Photobiol., A*, 2005, **176**, 129–135.
48 S. T. Andersen, M. Kyte, L. L. Andersen, O. J. Nielsen and M. P. Sulbaek Andersen, *Int. J. Chem. Kinet.*, 2018, **50**, 813–826.
49 Q. S. Li, X. D. Xu and S. Zhang, *Chem. Phys. Lett.*, 2004, **384**, 20–24.
50 A. Galano, *J. Phys. Chem. A*, 2007, **111**, 5086–5091.
51 Y. Tian, T. J. He, D. M. Chen and F. C. Liu, *Acta Phys.-Chim. Sin.*, 2008, **24**, 587–594.
52 M. Alihosseini, M. Vahedpour and M. Yousefian, *Comput. Theor. Chem.*, 2017, **1113**, 72–81.
53 Q.-S. Li and C. Y. Wang, *J. Comput. Chem.*, 2004, **25**, 251–257.
54 A. J. Ocaña, S. Blázquez, B. Ballesteros, A. Canosa, M. Antiñolo, J. Albaladejo and E. Jiménez, *Phys. Chem. Chem. Phys.*, 2018, **20**, 5865–5873.
55 A. J. Ocaña, S. Blázquez, A. Potapov, B. Ballesteros, A. Canosa, M. Antiñolo, L. Vereecken, J. Albaladejo and E. Jiménez, *Phys. Chem. Chem. Phys.*, 2019, **21**, 6942–6957.
56 S. Blázquez, D. González, E. M. Neeman, B. Ballesteros, M. Agúndez, A. Canosa, J. Albaladejo, J. Cernicharo and E. Jiménez, *Phys. Chem. Chem. Phys.*, 2020, **22**, 20562–20572.
57 E. Jiménez, B. Ballesteros, A. Canosa, T. M. Townsend, F. J. Maigler, V. Napal, B. R. Rowe and J. Albaladejo, *Rev. Sci. Instrum.*, 2015, **86**, 45108.
58 A. Canosa, A. J. Ocaña, M. Antiñolo, B. Ballesteros, E. Jiménez and J. Albaladejo, *Exp. Fluids*, 2016, **57**, 1–14.
59 A. J. Ocaña, E. Jiménez, B. Ballesteros, A. Canosa, M. Antiñolo, J. Albaladejo, M. Agúndez, J. Cernicharo, A. Zanchet, P. del Mazo, O. Roncero and A. Aguado, *Astrophys. J.*, 2017, **850**, 28.
60 S. Blázquez, D. González, A. García-Sáez, M. Antiñolo, A. Bergeat, F. Caralp, R. Mereau, A. Canosa, B. Ballesteros, J. Albaladejo and E. Jiménez, *ACS Earth Space Chem.*, 2019, **3**, 1873–1883.
61 B. R. Rowe, A. Canosa and D. E. Heard, *Uniform Supersonic Flows in Chemical Physics*, World Scientific, Europe, 2022.
62 M. Antiñolo, M. Agúndez, E. Jiménez, B. Ballesteros, A. Canosa, G. El Dib, J. Albaladejo and J. Cernicharo, *Astrophys. J.*, 2016, **823**, 25.
63 E. Jiménez, M. Antiñolo, B. Ballesteros, A. Canosa and J. Albaladejo, *Phys. Chem. Chem. Phys.*, 2016, **18**, 2183–2191.
64 E. Jiménez, B. Lanza, A. Garzón, B. Ballesteros and J. Albaladejo, *J. Phys. Chem. A*, 2005, **109**, 10903–10909.
65 E. Jiménez, B. Ballesteros, E. Martínez and J. Albaladejo, *Environ. Sci. Technol.*, 2005, **39**, 814–820.
66 J. Albaladejo, B. Ballesteros, E. Jiménez, Y. Díaz de Mera and E. Martínez, *Atmos. Environ.*, 2003, **37**, 2919–2926.
67 M. Antiñolo, E. Jiménez, A. Notario, E. Martínez and J. Albaladejo, *Atmos. Chem. Phys.*, 2010, **10**, 1911–1922.
68 D. González, A. Lema-Saavedra, S. Espinosa, E. Martínez-Núñez, A. Fernández-Ramos, A. Canosa, B. Ballesteros and E. Jiménez, *Phys. Chem. Chem. Phys.*, 2022, **24**, 23593–23601.
69 E. M. Neeman, D. González, S. Blázquez, B. Ballesteros, A. Canosa, M. Antiñolo, L. Vereecken, J. Albaladejo and E. Jiménez, *J. Chem. Phys.*, 2021, **155**, 034306.
70 D. González, B. Ballesteros, A. Canosa, J. Albaladejo and E. Jiménez, *Front. Astron. Space Sci.*, 2022, **8**, 1–11.
71 Y. Zhao and D. G. Truhlar, *J. Chem. Theory Comput.*, 2008, **4**, 1849–1868.
72 B. J. Lynch, Y. Zhao and D. G. Truhlar, *J. Phys. Chem. A*, 2003, **107**, 1384.
73 I. M. Alecu, J. Zheng, Y. Zhao and D. G. Truhlar, *J. Chem. Theory Comput.*, 2010, **6**, 2872–2887.
74 L. Guerrero-Méndez, A. Lema-Saavedra, E. Jiménez, A. Fernández-Ramos and E. Martínez-Núñez, *Phys. Chem. Chem. Phys.*, 2023, **25**, 20988–20996.
75 J.-D. Chai and M. Head-Gordon, *Phys. Chem. Chem. Phys.*, 2008, **10**, 6615–6620.
76 F. Weigend and R. Ahlrichs, *Phys. Chem. Chem. Phys.*, 2005, **7**, 3297–3305.
77 T. B. Adler, G. Knizia and H.-J. Werner, *J. Chem. Phys.*, 2007, **127**, 221106.
78 K. A. Peterson, T. B. Adler and H.-J. Werner, *J. Chem. Phys.*, 2008, **128**, 84102.
79 L. G. Gao, J. Zheng, A. Fernández-Ramos, D. G. Truhlar and X. Xu, *J. Am. Chem. Soc.*, 2018, **140**, 2906–2918.
80 Y. Georgievskii and S. J. Klippenstein, *J. Chem. Phys.*, 2005, **122**, 194103.
81 A. Fernández-Ramos, A. Ellingson, B. C. Garrett and D. G. Truhlar, *Rev. Comput. Chem.*, 2007, **23**, 125.
82 M. Page and J. W. McIver Jr., *J. Chem. Phys.*, 1988, **88**, 922–935.
83 Y.-Y. Chuang, J. C. Corchado and D. G. Truhlar, *J. Phys. Chem. A*, 1999, **103**, 1140–1149.
84 D. Ferro-Costas, D. G. Truhlar and A. Fernández-Ramos, *Comput. Phys. Commun.*, 2020, **256**, 107457.
85 K. M. Douglas, D. I. Lucas, C. Walsh, N. A. West, M. A. Blitz and D. E. Heard, *Astrophys. J., Lett.*, 2022, **937**, L16.
86 C. Sleiman, S. González, S. J. Klippenstein, D. Talbi, G. El Dib and A. Canosa, *Phys. Chem. Chem. Phys.*, 2016, **18**, 15118–15132.
87 R. Atkinson, D. L. Baulch, R. A. Cox, J. N. Crowley, R. F. Hampson, R. G. Hynes, M. E. Jenkin, M. J. Rossi, J. Troe and IUPAC Subcommittee, *Atmos. Chem. Phys.*, 2006, **6**, 3625–4055.
88 C. Castro and W. L. Karney, *Angew. Chem., Int. Ed.*, 2020, **59**, 8355–8366.
89 Y.-Y. Chuang and D. G. Truhlar, *J. Phys. Chem. A*, 1998, **102**, 242–247.
90 J. C. Gómez Martín, R. L. Caravan, M. A. Blitz, D. E. Heard and J. M. C. Plane, *J. Phys. Chem. A*, 2014, **118**, 2693–2701.
91 R. J. Shannon, M. A. Blitz, A. Goddard and D. E. Heard, *Nat. Chem.*, 2013, **5**, 745–749.
92 R. L. Caravan, R. J. Shannon, T. Lewis, M. A. Blitz and D. E. Heard, *J. Phys. Chem. A*, 2015, **119**, 7130–7137.
93 R. J. Shannon, R. L. Caravan, M. A. Blitz and D. E. Heard, *Phys. Chem. Chem. Phys.*, 2014, **16**, 3466–3478.

94 B. Nizamov and S. R. Leone, *J. Phys. Chem. A*, 2004, **108**, 1746–1752.
95 R. J. Hoobler and S. R. Leone, *J. Geophys. Res.: Planets*, 1997, **102**, 28717–28723.
96 K. M. Hickson, J.-C. Loison and V. Wakelam, *ACS Earth Space Chem.*, 2021, **5**, 824–833.
97 K. M. Hickson and J.-C. Loison, *J. Phys. Chem. A*, 2022, **126**, 3903–3913.
98 T. L. Nguyen, B. Ruscic and J. F. Stanton, *J. Chem. Phys.*, 2019, **150**, 084105.
99 M. Agúndez and V. Wakelam, *Chem. Rev.*, 2013, **113**, 8710–8737.
100 D. McElroy, C. Walsh, A. J. Markwick, M. A. Cordiner, K. Smith and T. J. Millar, *Astron. Astrophys.*, 2013 **550**, A36.
101 D. C. Clary, C. E. Dateo and D. Smith, *Chem. Phys. Lett.*, 1990, **167**, 1–6.
102 T. Su and W. J. Chesnavich, *J. Chem. Phys.*, 1982, **76**, 5183–5185.
103 W. A. Payne, P. S. Monks, F. L. Nesbitt and L. J. Stief, *J. Chem. Phys.*, 1996, **104**, 9808–9815.

